



Article

High-Performance Ppb Level NO₂ Gas Sensor Based on Colloidal SnO₂ Quantum Wires/Ti₃C₂T_x MXene Composite

Baohui Zhang¹, Chong Li¹ , Min Li², Chen Fu¹, Ran Tao¹ , Honglang Li^{3,4,5} and Jingting Luo^{1,*}

¹ Key Laboratory of Optoelectronic Devices and Systems of Education Ministry and Guangdong Province, College of Physics and Optoelectronic Engineering, Shenzhen University, Shenzhen 518060, China

² College of Electrical Engineering, Nanjing Vocational University of Industry Technology, Nanjing 210023, China

³ National Center of Nanoscience and Technology, Beijing 100190, China

⁴ GBA Research Innovation Institute for Nanotechnology, Guangzhou 510535, China

⁵ Guangdong Guangnaxin Technology Co., Ltd., Guangzhou 510535, China

* Correspondence: luojt@szu.edu.cn

Abstract: Nitrogen dioxide is one origin of air pollution from fossil fuels with the potential to cause great harm to human health in low concentrations. Therefore, low-cost, low-power-consumption sensors for low-concentration NO₂ detection are essential. Herein, heterojunction by SnO₂ quantum wires, a traditional metal oxide NO₂ sensing material, and Ti₃C₂T_x MXene, a novel type of 2D layered material, was synthesized using a simple solvothermal method for enhancing gas-sensing performance and reducing operating temperature. The operating temperature was reduced to 80 °C, with a best performance of 27.8 and a fast response and recovery time (11 s and 23 s, respectively). The SnO₂ and Ti₃C₂T_x MXene composite exhibits high speed and low detection limit due to the construction of the heterojunction with high conductive Ti₃C₂T_x MXene. The selectivity and stability of gas sensors are carried out. This could enable the realization of fast response, high-sensitivity, and selective NO₂ sensing under low operating temperatures.

Keywords: Ti₃C₂T_x MXene; SnO₂; gas sensor; NO₂; nanocomposite



Citation: Zhang, B.; Li, C.; Li, M.; Fu, C.; Tao, R.; Li, H.; Luo, J.

High-Performance Ppb Level NO₂ Gas Sensor Based on Colloidal SnO₂ Quantum Wires/Ti₃C₂T_x MXene Composite. *Nanomaterials* **2022**, *12*, 4464. <https://doi.org/10.3390/nano12244464>

Academic Editor: Lyubov G. Bulusheva

Received: 1 December 2022

Accepted: 13 December 2022

Published: 15 December 2022

Publisher's Note: MDPI stays neutral with regard to jurisdictional claims in published maps and institutional affiliations.



Copyright: © 2022 by the authors. Licensee MDPI, Basel, Switzerland. This article is an open access article distributed under the terms and conditions of the Creative Commons Attribution (CC BY) license (<https://creativecommons.org/licenses/by/4.0/>).

1. Introduction

The development of urbanization, industrialization, and modern agriculture greatly facilitates human daily life, while greatly disturbing the ecological environment. Nitrogen dioxide (NO₂) is a highly reactive and toxic gas generated from fossil fuels (heating, power, engines, chemical industry, etc.) [1,2]. It can lead to acid rain, and its salts are the main component of PM (particulate matter in the atmosphere) [3]. Even at low concentrations under 1 ppm, it can cause an increase in symptoms of bronchitis in asthmatic children and cause lung function damage due to its strong oxidizing properties [4–6]. In total, 92% of the global population lives in cities with air pollution exceeding limits from a WHO report [7], indicating the need for further monitoring and control of low-concentration air pollutant gases.

Gas sensors based on metal oxide semiconductors (MOS)—such as ZnO [8], SnO₂ [9], WO₃ [10], TiO₂ [11], etc.—have played an important role in NO₂ sensing due to their high sensitivity, fast response, and low cost. SnO₂, as a typical n-type MOS, is one of the most sensitive materials due to its high absorption [12,13]. Most SnO₂ sensors operate at a high temperature (300–400 °C) for better gas sensitivity, which not only reduces the sensor lifetime but also poses a risk of fire during long operation times [14–17]. At room temperature, the ultra-high resistance of SnO₂ sensors results in low response to NO₂ due to increased resistance as a result of surface reaction. Currently, improving gas adsorption and electronic transduction of MOS materials is a major problem in fabricating low-operating-temperature gas sensors. Recently, some researchers decreased the operating temperature of

SnO₂-based gas sensing materials by reducing dimensions and controlling the morphology of SnO₂ [18–21]. For example, Zhong et al. [22] synthesized SnO_{2-x} nanosheets, showing a high response of 16 to 5 ppm NO₂ at room temperature and taking more than 1000 s for recovery in 2019. In 2021, Hung et al. used SnO₂ nanowires as sensing material. They had 50 and 100 s response and recovery times, respectively, under UV light [23]. In the same year, Zhou et al. made hollow SnO₂ microspheres using colloidal nano SnO₂ for NO₂ sensing at room temperature, reaching a response of 10 to 10 ppm NO₂ and a fast recovery time of 65 s [24].

Reducing dimensions and controlling the morphology is an active pathway for reducing the operating temperature of SnO₂ gas sensors. The carrier transportation limited the electron injection for NO₂ desorption and resistance reduction. Low-dimensional layered materials with high mobility were used for improving response speed at low operating temperatures. In 2015, Li et al. [25] used rGO mixed with SnO₂ nanoparticles as a sensing material with fast response but slow recovery. Inaba et al. used SnO₂-decorated SWCNT as a sensing material, reaching a response of 19 at 1 ppm NO₂ under UV [26]. Ti₃C₂T_x, the first-layered MXene which is synthesized via HF etching of Ti₃AlC₂ using MAX by Gogosti in 2011, with rich active surface groups and ultra-high conductivity, has shown great attraction for ammonia and VOC sensing in recent research [27–30]. It was also used as a composite, with SnO₂ improving its gas sensing performance. Liu et al. made a SnO₂/Ti₃C₂T_x composite with response close to 50 ppb NO₂ at room temperature but full recovery at 100 °C [31]. Composites with 2D materials show potential for low-concentration and low-operating-temperature NO₂ sensors for environmental monitoring.

Herein, we processed SnO₂ quantum wires and Ti₃C₂T_x MXene composite for reducing operating temperature. Series mass of MXene was added for turning gas-sensing performance and operating temperature. Gas-sensing performance and characterizations were tested for explaining potential ppb-level NO₂-sensing mechanism. It has been found that Ti₃C₂T_x MXene provided a highly conductive pathway for improved charge transportation, resulting in high- and fast-response SnO₂/MXene composite NO₂ sensors at low operating temperatures.

2. Materials and Methods

2.1. Materials and Synthesis

All the reagents were utilized as supplied without additional purification treatment. The Ti₃AlC₂ powder was purchased from Jilin 11th Technology Co. Ltd. (Jilin, China). Oleic acid (OA) and oleyl amine (OLA) were brought from Alfa Aesar. LiF and SnCl₄·5H₂O were from Shanghai Aladdin Biochemical Technology Co., Ltd. (Shanghai, China). HCl, toluene, and ethanol were from Sinopharm Chemical Reagent Co., Ltd. (Shanghai, China) The resistivity of the DI water employed throughout the whole experiment was around 18 MΩ·cm.

All methods of synthesis and testing are shown in Figure 1. The pristine Ti₃C₂T_x MXene was prepared through the in situ HF generation etching method according to reports in the literature [27]. An amount of 1.65 g LiF was added to 15 mL HCl and 5 mL DI water mixture (forming 9M HCl at last) in a Teflon lining. 1 g of Ti₃AlC₂ powder was slowly added into the above solution in an ice bath, preventing the solution from overheating, and then magnetically stirred continuously for 24 h in a 40 °C oil bath. After etching, the product was washed and centrifuged repeatedly with DI water until the pH of the supernatant returned to 7. The Ti₃C₂T_x MXene was pumped, filtered, and dried at 60 °C under vacuum overnight, and powder was collected for composite.

The colloidal SnO₂ was synthesized using a simple solvothermal method, shown in Figure 1 [32]. Firstly, 0.7 g SnCl₄·5H₂O (2 mmol) was mixed in 20 mL of oleic (OA) and 1.5 mL of oleyl amine (OLA). Then, the mixture was ultrasonically dispersed for 30 min until transparent. Next, the mixture was transferred into a Teflon-lined steel autoclave with 10 mL ethanol to react at 180 °C for 3 h. After rapid cooling to room temperature, the mixture was precipitated with ethanol and redispersed in toluene three times. Ti₃C₂T_x

MXene was dissolved in ethanol (forming 3, 6, 9, 12 mg/mL for Moore ratios of 10%, 20%, 30%, and 40%, respectively, to SnO₂) for composite synthesis. Finally, all the precipitate was dispersed in toluene for sensor fabrication. These materials and sensors with differently treated materials were marked as SnO₂, ST3, ST6, ST9, and ST12, respectively.

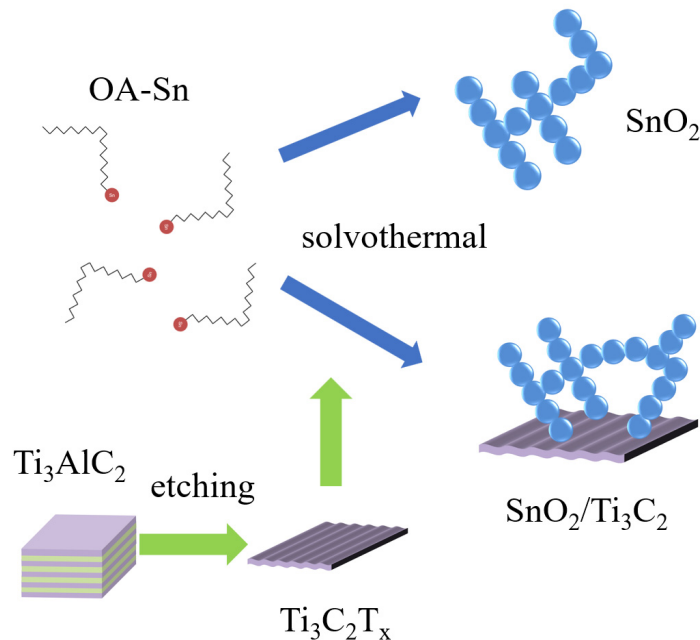


Figure 1. SnO₂ and SnO₂/Ti₃C₂T_x composite synthesis scheme.

2.2. Material Characterization

The crystal phase was analyzed with X-ray diffraction analysis (XRD; Rigaku D/Max 2550, Akishima, Japan) using Cu K α radiation ($\lambda = 1.5418 \text{ \AA}$) in the 2θ range of $5\text{--}80^\circ$. The microstructure was observed via scanning electron microscopy (SEM; Sigma 300 Zeiss, Oberkochen, Germany) with an acceleration voltage of 15 kV. The element ratio and spot pattern scanning analysis were tested using energy dispersive X-ray spectroscopy (EDS) with SEM. Transmission electron microscopy (TEM; FEI Tecnai G2 F20 S-Twin, Hillsboro, OR, USA) was conducted with an acceleration voltage of 200 kV. X-ray photoelectron spectroscopy (XPS) data were obtained on a Thermo Fisher Scientific K-Alpha (Waltham, MA, USA) with an Al source, and the sample was prepared via drop casting Ti₃C₂T_x MXene on Si substrate.

2.3. Gas Sensor Fabrication and Testing

Alumina ceramic plate with inter-digital Ag electrodes was used as the substrate of the gas sensor. Before film fabrication, devices were cleaned with acetone and absolute ethanol and then dried under nitrogen flow. The gas sensor was prepared via the spin-coating method. SnO₂ and SnO₂-MXene composite were dispersed in toluene, forming 20 mg/mL solution, were dropped onto the substrate, and then were spun at 2000 rpm for 30 s before being washed with methanol. These steps were repeated 3 times to form gas sensors. Then, the sensors were annealed at 300 °C for 3 h for surface OA removal.

The gas-sensing properties of the resistance sensor were evaluated using a Keithley 2400 digital source (Tektronix, Beaverton, OR, USA) meter with an 18 L chamber via the static sensing method. Temperature was raised with a heating plate and tested with a thermocouple. When the resistance of the sensors was stable, target gas with desired concentrations was injected into the chamber using syringes. As the sensor resistance reached a constant value, the chamber was opened for recovery in the atmosphere. The response of the gas sensor is defined as $S = \Delta R_g / R_a$, where R_a is the resistance of the sensor in air (base resistance) and ΔR_g is the resistance change of the sensor in the target gas.

The response time was defined as the time taken by the sensor to achieve 90% of the total resistance/frequency change in the case of gas adsorption. Similarly, the recovery time was defined as the time taken by the sensor response to reduce to 10% of its maximal value in the case of gas desorption.

3. Results

3.1. Materials Characterization

Figure 2 displays the XRD patterns of MAX phase Ti_3AlC_2 , $\text{Ti}_3\text{C}_2\text{T}_x$ MXene, SnO_2 , and composite. Ti_3AlC_2 MAX powder shows intense crystalline peaks at 19.12° , 34° , 36.72° , 39° , 41.74° , 56.42° , 60.18° , 70.38° , and 74.06° , which are indexed to the (004), (011), (013), (014), (015), (109), (110), (01 12), and (118) diffraction planes, respectively, in Figure 2a [33,34]. The $\text{Ti}_3\text{C}_2\text{T}_x$ peaks at 8.52° , 18.6° , and 28.7° indexed to the (002), (004), and (006) planes, respectively [27]. The peaks at 34.96° , 39.64° , and 45.96° were peaks of Ti_3C_2 and TiC which were over-etched. The reflection disappearance of highest (014) peak confirmed the Al was etched with HF. The small peaks between 35° and 45° correspond to the termination groups (–OH) and (–F), respectively, of MXene [35].

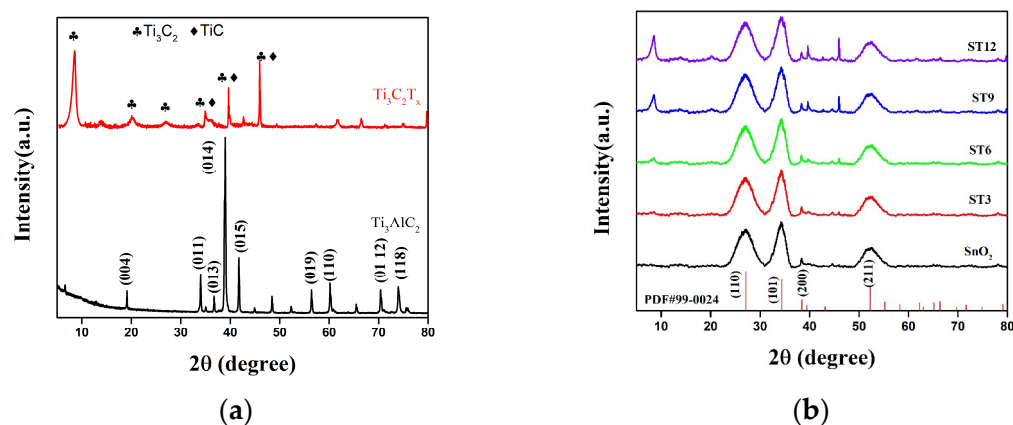


Figure 2. The X-ray diffraction patterns of (a) MAX and MXene, (b) SnO_2 , and their composites (ST3, ST6, ST9, and ST12).

The XRD pattern of SnO_2 showed reflection peaks at 26.58° , 33.86° , 33.94° , and 51.75° , corresponding to (110), (101), (200), and (211) planes, respectively, confirming its tetragonal rutile phase (JCPDS Card No #99-0024). The presence of the independent peaks of SnO_2 and $\text{Ti}_3\text{C}_2\text{T}_x$ MXene without any impurity peaks suggests the successful preparation of the composite (Figure 2b). The peak was almost invisible in the XRD pattern of ST3. Then, the peak intensity of $\text{Ti}_3\text{C}_2\text{T}_x$ MXene significantly increases with an increase in its concentration in ST composite.

Pure colloidal SnO_2 was shown in Figure 3a. It shows that colloidal SnO_2 was 2–3 nm diameter quantum dot necking in colloidal SnO_2 networks. With the addition of $\text{Ti}_3\text{C}_2\text{T}_x$ MXene (Figure 3b–e), colloidal SnO_2 networks saw epitaxial growth on the surface of $\text{Ti}_3\text{C}_2\text{T}_x$ MXene. The $\text{Ti}_3\text{C}_2\text{T}_x$ MXene sheets were not visible in ST3 composite. With an increase in $\text{Ti}_3\text{C}_2\text{T}_x$ MXene, the $\text{Ti}_3\text{C}_2\text{T}_x$ MXene sheets were clearer, and colloidal SnO_2 networks decreased on the $\text{Ti}_3\text{C}_2\text{T}_x$ MXene. SAED (selected area electron diffraction) of SnO_2 , ST9, and ST12 is shown in the corresponding graph. Furthermore, the lattice spacings were found to be 0.334 and 0.267 nm, which are consistent with the (110) and (101) planes of rutile SnO_2 [32], respectively (Figure 3f). Figure 3g shows the interface of $\text{Ti}_3\text{C}_2\text{T}_x$ MXene and colloidal SnO_2 networks of ST9; the MXene surface displayed fully epitaxial growth with SnO_2 . The interface of ST12 in Figure 3h shows that the surface was not full filled with SnO_2 .

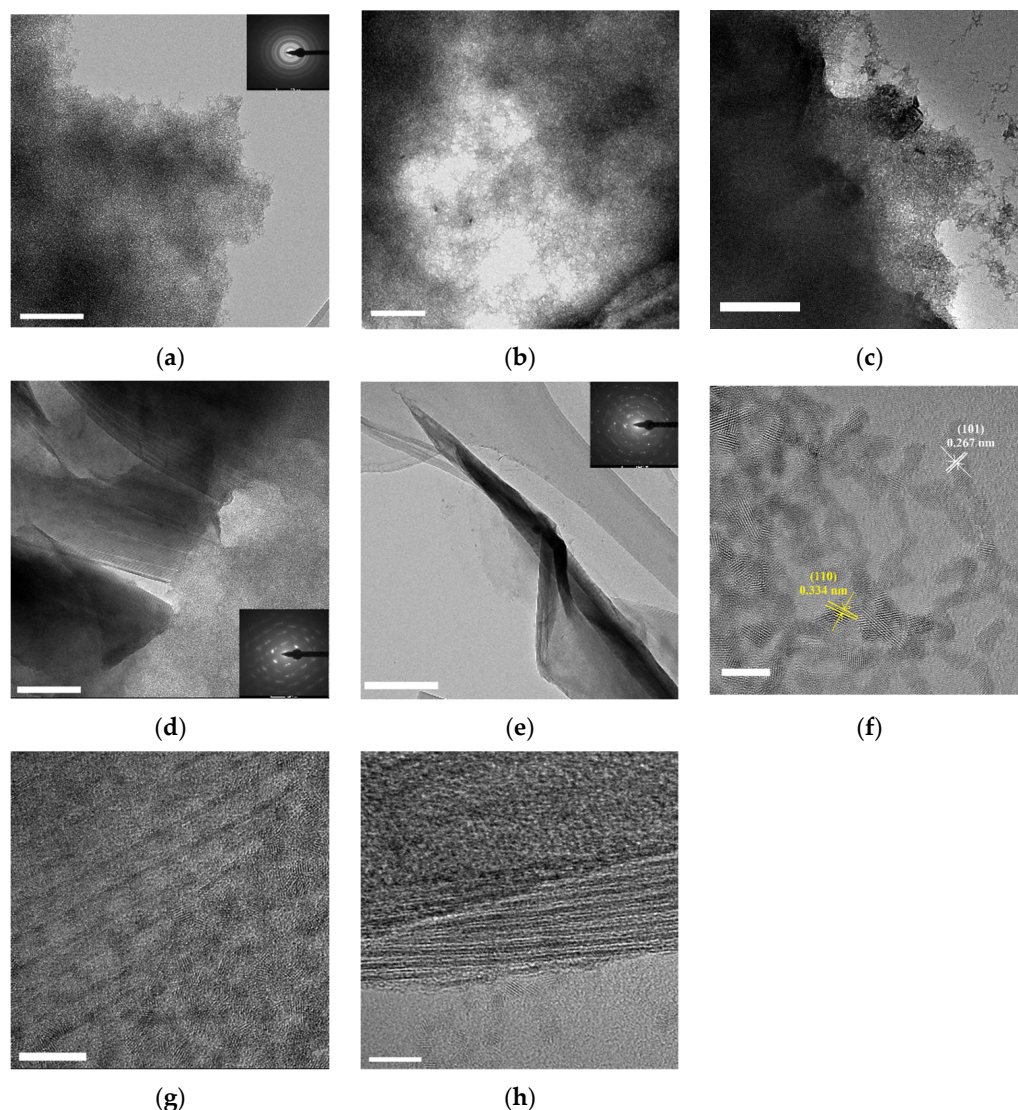


Figure 3. TEM of (a) colloidal SnO₂, (b) ST3, (c) ST6, (d) ST9, (e) ST12 (scale bar 200 nm). High resolution TEM of (f) SnO₂, (g) ST9, and (h) ST12 (scale bar 5 nm).

The morphology of the as-prepared samples has been analyzed through employing SEM. As plotted in Figure 4a, the Ti₃C₂T_x MXene shows organ-like stack sheets after the HF etching. Figure 4b shows the morphology of pure SnO₂ film. It shows a smooth colloidal film with some small stacks. ST3 film in Figure 4c has more stacks on the film surface for Ti₃C₂T_x MXene adding. With an increase in Ti₃C₂T_x MXene, the film turns rough. And the ST12 film shows sheets more like the Ti₃C₂T_x MXene film (Figure 4f).

Figure 5 shows the XPS survey and high-resolution spectra of colloidal SnO₂, Ti₃C₂T_x MXene, and ST9 composites. Colloidal SnO₂ shows C–C bonds at 281.2 eV from surface OA ligand (Figure 5b). The Ti₃C₂T_x MXene shows two similar-intensity peaks at 281.2 and 284.2 eV ascribed to Ti–C and C–C bonds [36,37], respectively. The ST9 composite shows a weak Ti–C bond, and OA ligand was at the composite surface, introducing more C–C groups. F 1s high-resolution spectra with a binding energy of 686 eV was shown in Figure 5c. After mixture, the F 1s peak becomes weaker and redshifts. As shown in Figure 5d, the presence of two split peaks (Sn 3d5/2 and Sn 3d3/2 at 487.1 and 495.6 eV, respectively) confirms the formation of SnO₂. The Sn peaks of ST9 are also weaker and slightly less redshifted than those of pure SnO₂. The four pairs of peaks of Ti 2p centralized at 454.9 and 461.1, 455.8 and 461.4, 457.1 and 462.9, and 458.9 and 464.5 eV correspond to Ti–C, C–Ti–OH, C–Ti–O, and TiO₂, respectively [38,39]. TiO₂ and Ti–O groups strengthen

the other active functional surface Ti groups against oxidation while using the solvothermal method (Figure 5e,f). The O 1s peaks at 530.7 and 532.5 eV can be assigned to the lattice O (O_L , Sn–O–Sn) and chemically absorbed O (O_a), respectively (Figure 5g). Figure 5h shows the O 1s peaks of $Ti_3C_2T_x$ MXene at 529.9 and 532.2 eV for Ti–O and Ti–C–O groups, respectively [40,41]. In composite, the lattice O of SnO_2 was the main oxide state and absorbed and Ti–C–O followed. There were still Ti–O groups on the composite.

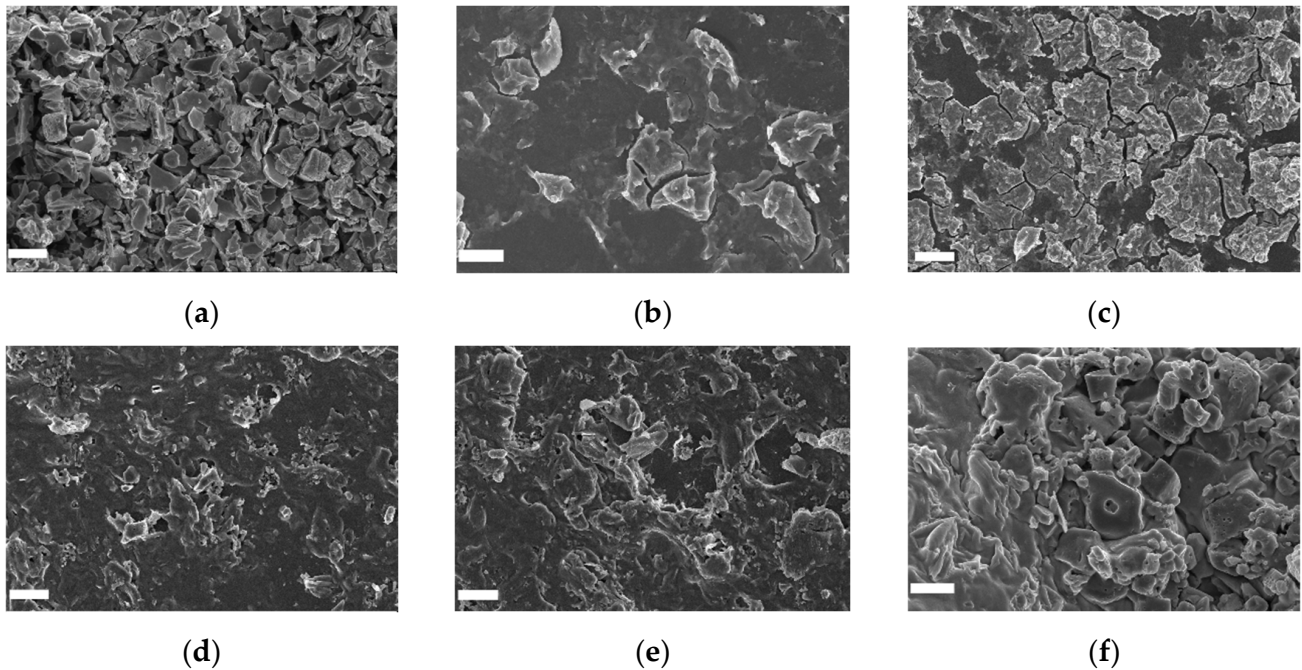


Figure 4. Film morphology of (a) $Ti_3C_2T_x$ MXene, (b) SnO_2 , (c) ST3, (d) ST6, (e) ST9, and (f) ST12 by SEM (scale bar 10 μm).

3.2. Gas-Sensing Performance

Figure 6a displays resistance curves of ST9 sensor towards 10 ppm NO_2 under series operating temperature. The resistance increases after exposure to NO_2 for SnO_2 as a p-type semiconductor. With the operating temperature increasing, the baseline resistance decreases from 40.9 M Ω to 8.1 M Ω due to high carrier transportation under high temperature. The resistance under target gas decreases, but the response shows an increasing trend at first below 80 $^{\circ}C$ and a decreasing trend as operating temperature increases from 15.6 to 27.8 in the calculated response curves in Figure 6b. Figure 6c compares the response and recovery time of ST9 sensor towards 10 ppm NO_2 under different operating temperature. As operating temperature increases, the response and recovery changes quickly from over 100 s to around 10 s. The relationship of operating temperature to R_a and R_g and response towards 10 ppm NO_2 was calculated and summarized in Figure 6d–f, respectively. It shows that as the operating temperature and the MXene ratio increase, gas sensor resistance decreases. As the $Ti_3C_2T_x$ MXene increases, the optimal working temperature decreases. The response of pure SnO_2 sensors still increases when the operating temperature increases up to 120 $^{\circ}C$. The ST3 and ST6 sensor shows a best performance at 100 $^{\circ}C$. ST9 and ST12 sensors shows the highest responses at 80 and 60 $^{\circ}C$, respectively. The 2D $Ti_3C_2T_x$ MXene sheets introduce an effective method of decreasing operating temperature.

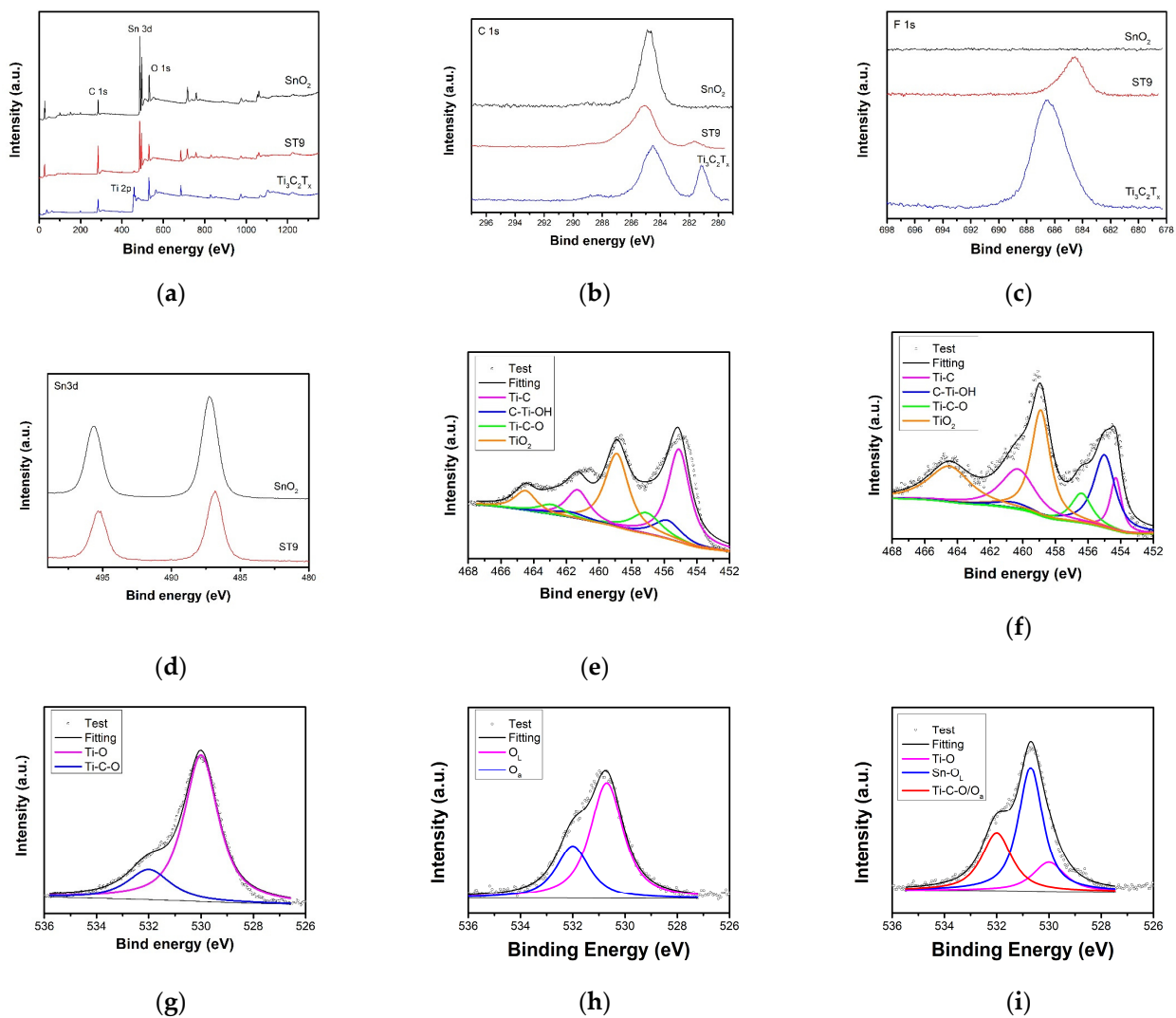


Figure 5. (a) XPS survey and high-resolution spectra of SnO₂, Ti₃C₂T_x MXene, and ST9 composite. High-resolution XPS spectra of (b) C 1s, (c) F 1s, and (d) Sn 3d. Ti 2p spectra of (e) Ti₃C₂T_x MXene and (f) ST9. O 1s spectra of (g) SnO₂, (h) Ti₃C₂T_x MXene, and (i) ST9.

Figure 7a presents the resistance curves of ST9 sensor under 80 °C towards series NO₂ (10 ppm to 0.2 ppm). As the concentration decreases, the response becomes smaller and the response speed slower. The ST9 sensor showed the highest response of 27.8 toward 10 ppm NO₂ at 80 °C, with response and recovery times of 11 and 23 s, respectively (Figure 7b). The NO₂-sensing performance compared to that of other research was listed in Table 1. Figure 7c exhibits the linear fitting curve of the pure SnO₂ and ST9 sensor response to NO₂ concentration. The theoretical detection limits of the sensors were estimated to be 20 ppb (ST9) and 100 ppb (SnO₂) according to the least-squares method. Repeatability and long-term stability are also two important aspects in gas-sensing applications. Figure 7d shows the repeat curves of ST9 sensor to 10 ppm NO₂ 80 °C for 6 cycles, indicating a highly stable sensing performance. Furthermore, the long-term responses for a month of pure SnO₂ and ST9 sensor to 10 ppm NO₂ show a slight reduction under 10% (Figure 7e), indicating good long-term stability. The responses of pure SnO₂ and ST9 sensor to 10 ppm NO₂, CO, NH₃, SO₂, CH₄ and ethanol were shown in Figure 7f. The response towards NO₂ was much higher than the other gases, indicating that the SnO₂ and ST9 had high selectivity to NO₂, and selectivity of ST9 also improved to pure SnO₂.

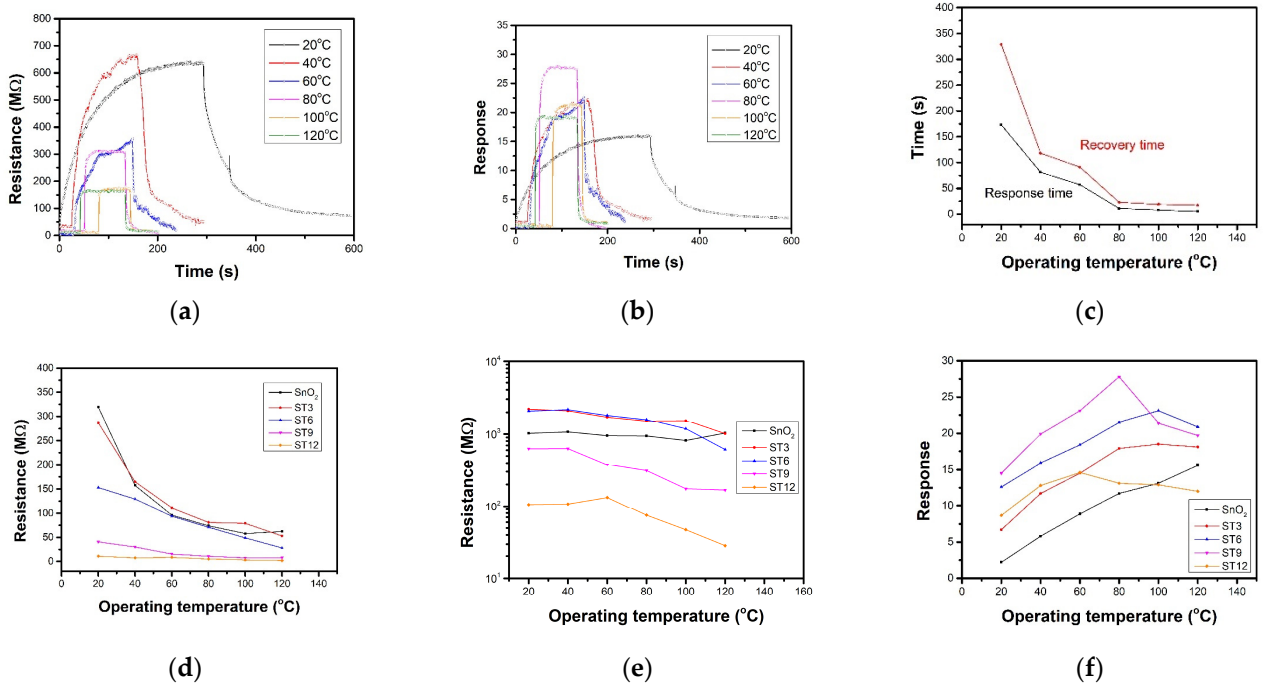


Figure 6. (a) Resistance and (b) response curves of ST9 sensor under different operating temperatures. (c) Response and recovery times of ST9 sensor under different operating temperatures. Target gas was 10 ppm NO₂. (d) R_a, (e) R_g, and (f) responses of gas sensors under different operating temperatures.

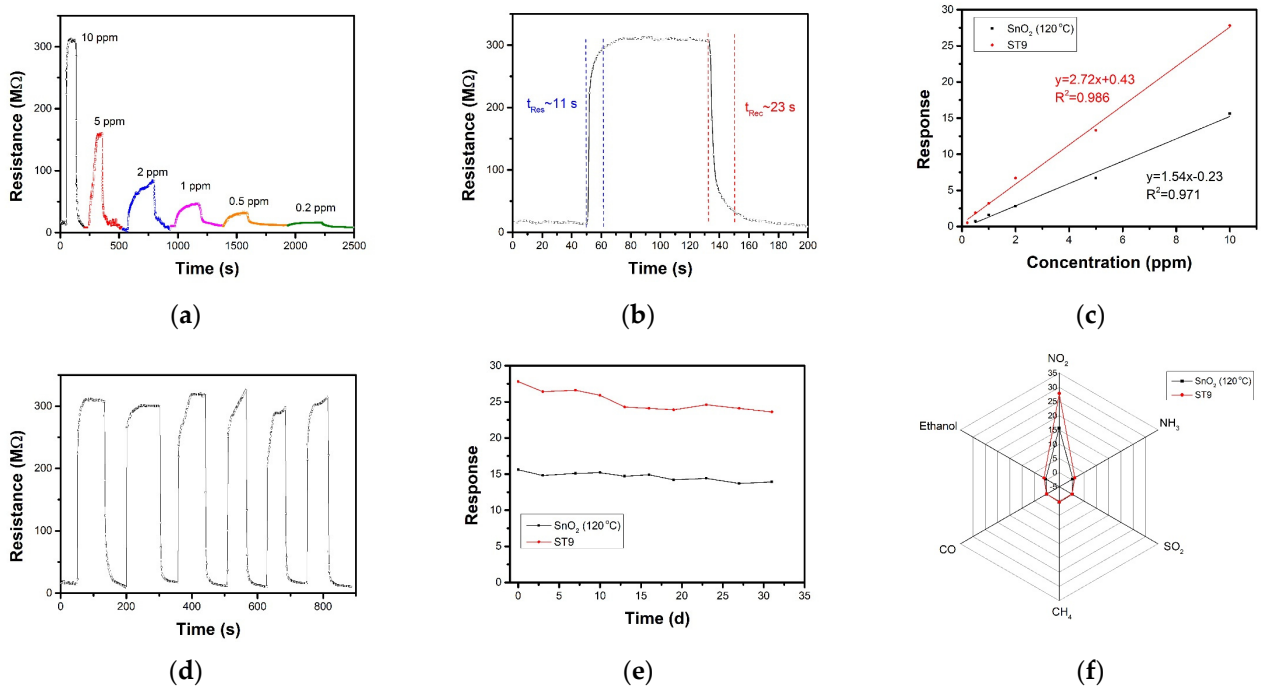


Figure 7. (a) Resistance curve of ST9 sensor towards series concentration NO₂ at 80 °C. (b) Dependence of sensor response and the linear fitting upon NO₂ concentration of ST9 sensor at 80 °C and SnO₂ sensor at 120 °C. (c) Response and recovery time of ST9 sensor towards 10 ppm NO₂ at 80 °C; (d) repeat curves of ST9 sensor towards 10 ppm NO₂ at 80 °C. (e) Stability in a month of SnO₂ and ST9 sensors towards 10 ppm NO₂. (f) Selectivity of SnO₂ and ST9 sensors toward 10 ppm NO₂, NH₃, SO₂, CH₄, CO, and ethanol.

Table 1. NO₂-gas-sensing performance of SnO₂-based sensors.

Materials	Response	Operating Temperature (°C)	Response/Recovery Time	LoD	Reference
SnO _{2-x} nanosheets	16@5 ppm	RT	331 s/1057 s	-	[22]
SnO ₂ nanowires	50@5 ppm	RT(UV)	420 s/100 s	100 ppb	[23]
SnO ₂ hollow microspheres	10@10 ppm	RT	17 s/65 s	26 ppb	[24]
Bio-templated SnO ₂ channels	35.9@100 ppm	RT	2.67 s/13 s	10 ppb	[42]
leaf-like SnO ₂	7@0.5 ppm	65	10 min/46 min	-	[43]
rGO/SnO ₂	84.5%@0.5 ppm	120	22 s/125 s	-	[44]
CNT/SnO ₂	0.59@0.5 ppm	RT	~40 s/~200 s	100 ppb	[45]
SWCNT/SnO ₂ nanoparticles	18@1 ppm	RT(UV)	200 s/-	1 ppb	[26]
MoS ₂ /SnO ₂	34@100 ppm	RT	2.2 s/11 s	10 ppb	[46]
Ti ₃ C ₂ /SnO ₂	1.57@10 ppm	RT	~300 s/~100 s (100 °C)	50 ppb	[29]
Ti ₃ C ₂ T _x /SnO ₂	27.8@10 ppm	80	11 s/23 s	20 ppb	This work

3.3. Gas-Sensing Mechanism

Based on its gas-sensing performance and material characterizations, the gas-sensing mechanism of SnO₂/Ti₃C₂T_x MXene composite has been hypothesized. The SnO₂ sensing mechanism is traditionally analyzed using the surface control model [47], which is based on the interaction between chemisorbed oxygen species and target gases on the surface of SnO₂. Generally, oxygen in ambient air adsorbed on metal oxide surfaces converted to O₂⁻, O⁻, and O²⁻ by capturing electrons near the valence band. In our work, O₂⁻ and O⁻ were the main absorbed oxygen states on the SnO₂ surface following the reaction [47]:



Normally, the O²⁻ was mostly formed above 400 °C. The surface-absorbed oxygen formed a depletion zone on the SnO₂ surface (blue area in Figure 8). This caused the carrier balance to begin forming the resistance of gas sensors. When exposed to NO₂, the surface-absorbed oxygen reacts with NO₂ per follow equation [48]:



This reaction introduces the consumption of electronics forming a deeper depletion zone on the SnO₂ surface, leading the resistance of gas sensor increase.

With the addition of Ti₃C₂T_x MXene, SnO₂/Ti₃C₂T_x MXene heterostructures are formed with Schottky barriers. The Fermi level of SnO₂ was at 4.5 eV [49], higher than the Ti₃C₂T_x MXene work function (~3.9 eV) [50]. The Fermi level balance leading electron injecting from the MXene to SnO₂ and formed the band bending. Another electron depletion region between the interface of SnO₂ and Ti₃C₂T_x MXene was formed. When exposed to NO₂, two depletion regions were both widened for electron consumption, enhancing NO₂ sensing performance. The Ti₃C₂T_x MXene sheet introduced folded and stacked multilayer into the film, which offered a large number of active sites and gas molecule transport channels for the adsorption of oxygen and NO₂, thus improving the NO₂-sensing response. In addition, the high conductivity of Ti₃C₂T_x MXene formed a carrier transportation channel during the sensing process and decreased the response and recovery time. The performances of ST3 and ST6 sensors were improved, but the Ti₃C₂T_x MXene was not enough for carrier transportation. The ST12 sensor response decrease was due to the Ti₃C₂T_x MXene surface not being fully grown, transporting more electrons for band balance and reflecting Ti₃C₂T_x MXene p-type response to gases, opposite to the n-type SnO₂.

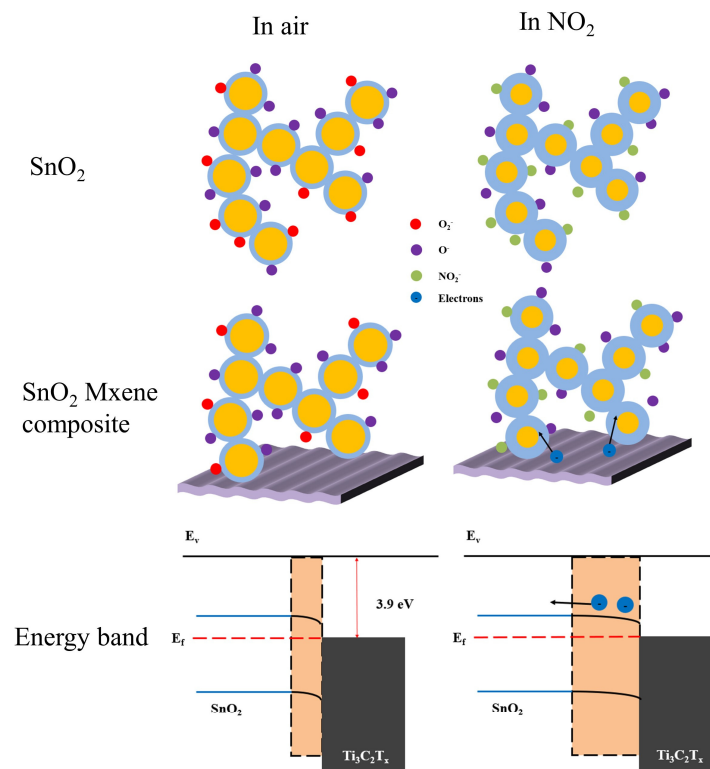


Figure 8. Schematic illustration of NO_2 -sensing mechanism for SnO_2 and $\text{SnO}_2\text{-Ti}_3\text{C}_2\text{T}_x$ composite sensor.

4. Conclusions

In summary, SnO_2 quantum wires and $\text{Ti}_3\text{C}_2\text{T}_x$ MXene composites with different ratios were synthesized using the one-step solvothermal method. SnO_2 quantum wire epitaxial growth occurred on the surface of $\text{Ti}_3\text{C}_2\text{T}_x$ MXene. $\text{Ti}_3\text{C}_2\text{T}_x$ MXene was oxidized during the solvothermal method. The molar ratio was 30% (MXene); the marked ST9 sensor showed the best response of 27.8 to 10 ppm NO_2 at 80 °C, with 11 s and 23 s of response and recovery time, respectively. The response of ST9 sensor was 2 times to pure SnO_2 at an operating temperature of 120 °C. The ST9 sensor could detect NO_2 as low as 20 ppb in theory with excellent selectivity. The potential gas-sensing mechanism of $\text{SnO}_2/\text{Ti}_3\text{C}_2\text{T}_x$ MXene composite has been hypothesized to be the heterostructure enhancing the carrier transfer into SnO_2 , enhancing surface reaction and sufficient carrier supplied by the high conductivity of $\text{Ti}_3\text{C}_2\text{T}_x$ MXene.

Author Contributions: B.Z. and C.L. completed most of the experiments and wrote the draft. B.Z. and M.L. designed the experiments. C.F., R.T., H.L., and J.L. made significant contributions to the revision of the experiment design and manuscript editing. M.L. and J.L. provided experimental support. All authors have read and agreed to the published version of the manuscript.

Funding: This research was funded by the Key Research and Development Program of Guangdong Province (Grant No.: 2020B0101040002), Special Projects in Key Fields of Colleges in Guangdong Province (2020ZDZX2007), Research Project in Fundamental and Application Fields of Guangdong Province (2020A1515110561), Guangdong Basic and Applied Basic Research Foundation (2019A1515111199), Shenzhen Science & Technology Project (Grant No. JCYJ20180507182106754, JCYJ20180507182439574, RCBS20200714114918249, GJHZ20200731095803010), National Natural Science Foundation of China (Grant No. 62004100), and Natural Science Foundation of Nanjing Vocational University of Industry Technology (Grant No. YK19-02-06).

Data Availability Statement: All data, models, and codes generated or used during the study appear in the submitted article.

Acknowledgments: We thank the College of Physics and Optoelectronic Engineering, Shenzhen University for the use of characterization equipment.

Conflicts of Interest: The authors declare no conflict of interest.

References

1. Kumunda, C.; Adekunle, A.S.; Mamba, B.B.; Hlongwa, N.W.; Nkambule, T.T.I. Electrochemical Detection of Environmental Pollutants Based on Graphene Derivatives: A Review. *Front. Mater.* **2021**, *7*, 616787. [[CrossRef](#)]
2. Mirzaei, A.; Ansari, H.R.; Shahbaz, M.; Kim, J.Y.; Kim, H.W.; Kim, S.S. Metal Oxide Semiconductor Nanostructure Gas Sensors with Different Morphologies. *Chemosensors* **2022**, *10*, 289. [[CrossRef](#)]
3. Li, K.; Luo, Y.Y.; Liu, B.; Gao, L.; Duan, G.T. High-performance NO₂-gas sensing of ultrasmall ZnFe₂O₄ nanoparticles based on surface charge transfer. *J. Mater. Chem. A* **2019**, *10*, 5539–5551. [[CrossRef](#)]
4. Mallapaty, S. The coronavirus is most deadly if you are old and male. *Nature* **2020**, *585*, 16–17. [[CrossRef](#)] [[PubMed](#)]
5. Sharma, B.; Sharma, A.; Myung, J.H. Selective ppb-level NO₂ gas sensor based on SnO₂-boron nitride nanotubes. *Sens. Actuators B Chem.* **2021**, *331*, 129464. [[CrossRef](#)]
6. Liu, D.; Ren, X.W.; Li, Y.S.; Tang, Z.L.; Zhang, Z.T. Nanowires-assembled WO₃ nanomesh for fast detection of ppb-level NO₂ at low temperature. *J. Adv. Ceram.* **2020**, *9*, 17–26. [[CrossRef](#)]
7. Ming, Y.; Deng, H.; Wu, X. The negative effect of air pollution on people's pro-environmental behavior. *J. Bus. Res.* **2022**, *142*, 72–87. [[CrossRef](#)]
8. Agarwal, S.; Rai, P.; Gatell, E.N.; Llobet, E.; Guell, F.; Kumar, M.; Awasthi, K. Gas sensing properties of ZnO nanostructures (flowers/rods) synthesized by hydrothermal method. *Sens. Actuators B Chem.* **2019**, *292*, 24–31. [[CrossRef](#)]
9. Wang, X.; Gao, M. Porous CO₃O₄/SnO₂ quantum dot (QD) hetero-structures with abundant oxygen vacancies and CO₂⁺ ions for highly efficient gas sensing and oxygen evolution reaction. *Nanoscale* **2018**, *10*, 12045. [[CrossRef](#)]
10. Liu, W.; Xu, L.; Sheng, K.; Chen, C.; Zhou, X.Y.; Dong, B.; Bai, X.; Zhang, S.; Lu, G.Y.; Song, H.W. APTES-functionalized thin-walled porous WO₃ nanotubes for highly selective sensing of NO₂ in a polluted environment. *J. Mater. Chem. A* **2018**, *6*, 10976–10989. [[CrossRef](#)]
11. Galstyan, V.; Ponzoni, A.; Khnlmanov, I.; Natile, M.M.; Comini, E.; Nematov, S.; Sberveglieri, G. Investigation of reduced graphene oxide and Nb-doped TiO₂ nanotube hybrid structure to improve gas sensing response and selectivity. *ACS. Sens.* **2019**, *4*, 2094–2100. [[CrossRef](#)]
12. Wang, Z.Y.; Han, T.Y.; Fei, T.; Liu, S.; Zhang, T. Investigation of microstructure effect on NO₂ sensors based on SnO₂ nanoparticles/reduced graphene oxide hybrids. *ACS Appl. Mater. Interfaces* **2018**, *10*, 41773–41783. [[CrossRef](#)]
13. Kou, X.Y.; Xie, N.; Chen, F.; Wang, T.S.; Guo, L.L.; Wang, C.; Wang, Q.J.; Ma, J.; Sun, Y.F.; Zhang, H.; et al. Superior acetone gas sensor based on electrospun SnO₂ nanofibers by Rh doping. *Sens. Actuators B Chem.* **2018**, *256*, 861–869. [[CrossRef](#)]
14. Zhang, J.; Liu, X.H.; Neri, G.; Pinna, N. Nanostructured materials for roomtemperature gas sensors. *Adv. Mater.* **2016**, *28*, 795–831. [[CrossRef](#)]
15. Mohanta, D.; Ahmaruzzaman, M. Novel Ag-SnO₂-βC₃N₄ ternary nanocomposite based gas sensor for enhanced low-concentration NO₂ sensing at room temperature. *Sens. Actuators B Chem.* **2021**, *326*, 128910. [[CrossRef](#)]
16. Zheng, S.L.; Sun, J.Y.; Hao, J.Y.; Sun, Q.; Wan, P.; Li, Y.; Zhou, X.; Yuan, Y.; Zhang, X.; Wang, Y. Engineering SnO₂ nanorods/ethylenediamine-modified graphene heterojunctions with selective adsorption and electronic structure modulation for ultrasensitive room-temperature NO₂ detection. *Nanotechnology* **2021**, *32*, 155505. [[CrossRef](#)] [[PubMed](#)]
17. Wei, B.Y.; Hsu, M.C.; Su, P.G.; Lin, H.M.; Wu, R.J.; Lai, H.J. A novel SnO₂ gas sensor doped with carbon nanotubes operating at room temperature. *Sens. Actuators B Chem.* **2004**, *11*, 81–89. [[CrossRef](#)]
18. Wang, C.X.; Cai, D.P.; Liu, B.; Li, H.; Wang, D.D.; Liu, Y.; Wang, L.L.; Wang, Y.R.; Li, Q.H.; Wang, T.H. Ethanol-sensing performance of tin dioxide octahedral nanocrystals with exposed high-energy {111} and {332} facets. *J. Mater. Chem. A* **2014**, *2*, 10623–10628. [[CrossRef](#)]
19. Han, X.G.; Jin, M.S.; Xie, S.F.; Kuang, Q.; Jiang, Z.Y.; Jiang, Y.Q.; Xie, Z.X.; Zheng, L.S. Synthesis of tin dioxide octahedral nanoparticles with exposed high-energy {221} facets and enhanced gas-sensing properties. *Angew. Chem. Int. Ed.* **2009**, *48*, 9180–9183. [[CrossRef](#)] [[PubMed](#)]
20. Zhang, L.Z.; Shi, J.N.; Huang, Y.H.; Xu, H.Y.; Xu, K.W.; Chu, P.K.; Ma, F. Octahedral SnO₂/graphene composites with enhanced gas-sensing performance at room temperature. *ACS Appl. Mater. Interfaces* **2019**, *11*, 12958–12967. [[CrossRef](#)] [[PubMed](#)]
21. Xu, R.; Zhang, L.X.; Li, M.W.; Yin, Y.Y.; Yin, J.; Zhu, M.Y.; Chen, J.J.; Wang, Y.; Bie, L.J. Ultrathin SnO₂ nanosheets with dominant high-energy {001} facets for low temperature formaldehyde gas sensor. *Sens. Actuators B Chem.* **2019**, *289*, 186–194. [[CrossRef](#)]
22. Zhong, Y.; Li, W.; Zhao, X.; Jiang, X.; Lin, S.; Zhen, Z.; Chen, W.; Xie, D.; Zhu, H. High-Response Room-Temperature NO₂ Sensor and Ultrafast Humidity Sensor Based on SnO₂ with Rich Oxygen Vacancy. *ACS Appl. Mater. Interfaces* **2019**, *11*, 13441–13449. [[CrossRef](#)] [[PubMed](#)]

23. Hung, N.M.; Hung, C.M.; Duy, N.V.; Hoa, N.D.; Hong, H.S.; Dang, T.K.; Viet, N.N.; Thong, L.V.; Phuoc, P.H.; Van Hieu, N. significantly enhanced NO₂ gas-sensing performance of nanojunction-networked SnO₂ nanowires by pulsed UV-radiation. *Sens. Actuators A Phys.* **2021**, *327*, 112759. [[CrossRef](#)]
24. Zhou, L.; Hu, Z.; Li, H.Y.; Liu, J.; Zeng, Y.; Wang, J.; Huang, Y.; Miao, L.; Zhang, G.; Huang, Y.; et al. Template-Free Construction of Tin Oxide Porous Hollow Microspheres for Room-Temperature Gas Sensors. *ACS Appl. Mater. Interfaces* **2021**, *13*, 25111–25120. [[CrossRef](#)] [[PubMed](#)]
25. Li, L.; He, S.; Liu, M.; Zhang, C.; Chen, W. Three-Dimensional Mesoporous Graphene Aerogel-Supported SnO₂ Nanocrystals for High-Performance NO₂ Gas Sensing at Low Temperature. *Anal. Chem.* **2015**, *87*, 1638–1645. [[CrossRef](#)]
26. Inaba, M.; Oda, T.; Kono, M.; Phansiri, N.; Morita, T.; Nakahara, S.; Nakano, M.; Suehiro, J. Effect of mixing ratio on NO₂ gas sensor response with SnO₂-decorated carbon nanotube channels fabricated by one-step dielectrophoretic assembly. *Sens. Actuators B Chem.* **2021**, *344*, 130257. [[CrossRef](#)]
27. Naguib, M.; Kurtoglu, M.; Presser, V.; Lu, J.; Niu, J.; Heon, M.; Hultman, L.; Gogotsi, Y.; Barsoum, M.W. Two-dimensional nanocrystals produced by exfoliation of Ti₃AlC₂. *Adv. Mater.* **2011**, *23*, 4248–4253. [[CrossRef](#)]
28. Ranjith, K.S.; Vilian, A.T.E.; Ghoreishian, S.M.; Umapathi, R.; Hwang, S.K.; Oh, C.W.; Huh, Y.S.; Han, Y.K. Hybridized 1D–2D MnMoO₄–MXene nanocomposites as high-performing electrochemical sensing platform for the sensitive detection of dihydroxybenzene isomers in wastewater samples. *J. Hazard. Mater.* **2021**, *421*, 126775. [[CrossRef](#)]
29. Umapathi, R.; Ghoreishian, S.M.; Sonwal, S.; Rani, G.M.; Huh, Y.S. Portable electrochemical sensing methodologies for on-site detection of pesticide residues in fruits and vegetables. *Coordin. Chem. Rev.* **2022**, *453*, 214305. [[CrossRef](#)]
30. Aghaei, S.M.; Aasi, A.; Panchapakesan, B. Experimental and Theoretical Advances in MXene-Based Gas Sensors. *ACS Omega* **2021**, *6*, 2450–2461. [[CrossRef](#)]
31. Liu, S.; Wang, M.; Ge, C.; Lei, S.; Hussain, S.; Wang, M.; Qiao, G.; Liu, G. Enhanced room-temperature NO₂ sensing performance of SnO₂/Ti₃C₂ composite with double heterojunctions by controlling co-exposed {221} and {110} facets of SnO₂. *Sens. Actuators B Chem.* **2022**, *365*, 131919. [[CrossRef](#)]
32. Xu, X.; Zhuang, J.; Wang, X. SnO₂ quantum dots and quantum wires: Controllable synthesis, self-assembled 2D architectures, and gas-sensing properties. *J. Am. Chem. Soc.* **2008**, *130*, 12527–12535. [[CrossRef](#)]
33. Chlubny, L.; Lis, J.; Chabior, K.; Chachlowska, P.; Kapusta, C. Processing and properties of MAX phases-based materials using SHS technique. *Arch. Metall. Mater.* **2015**, *60*, 859–863. [[CrossRef](#)]
34. Wang, H.; Wu, Y.; Zhang, J.; Li, G.; Huang, H.; Zhang, X.; Jiang, Q. Enhancement of the electrical properties of MXene Ti₃C₂ nanosheets by post-treatments of alkalization and calcination. *Mater. Lett.* **2015**, *160*, 537–540. [[CrossRef](#)]
35. Hermawan, A.; Zhang, B.; Taufik, A.; Asakura, Y.; Hasegawa, T.; Zhu, J.; Shi, P.; Yin, S. CuO nanoparticles/Ti₃C₂T_x MXene hybrid nanocomposites for detection of toluene gas. *ACS Appl. Nano Mater.* **2020**, *3*, 4755–4766. [[CrossRef](#)]
36. Wang, B.; Wang, M.; Liu, F.; Zhang, Q.; Yao, S.; Liu, X.; Huang, F. Ti₃C₂: An Ideal Cocatalyst? *Angew. Chem. Int. Ed.* **2020**, *59*, 1914–1918. [[CrossRef](#)]
37. Nam, S.; Umrao, S.; Oh, S.; Shin, K.H.; Park, H.S.; Oh, I. Sonochemical self-growth of functionalized titanium carbide nanorods on Ti₃C₂ nanosheets for high capacity anode for lithium-ion batteries. *Compos. Part B Eng.* **2020**, *181*, 107583. [[CrossRef](#)]
38. Xiu, L.; Wang, Z.; Yu, M.; Wu, X.; Qiu, J. Aggregation-resistant 3D MXene-based architecture as efficient bifunctional electrocatalyst for overall water splitting. *ACS Nano* **2018**, *12*, 8017–8028. [[CrossRef](#)] [[PubMed](#)]
39. Chae, Y.; Kim, S.J.; Cho, S.Y.; Choi, J.; Maleski, K.; Lee, B.J.; Jung, H.T.; Gogotsi, Y.; Lee, Y.; Ahn, C.W. An investigation into the factors governing the oxidation of two dimensional Ti₃C₂ MXene. *Nanoscale* **2019**, *11*, 8387–8393. [[CrossRef](#)]
40. Chen, W.Y.; Lai, S.; Yen, C.; Jiang, X.; Peroulis, D.; Stanciu, L.A. Surface functionalization of Ti₃C₂T_x MXene with highly reliable superhydrophobic protection for volatile organic compounds sensing. *ACS Nano* **2020**, *14*, 11490–11501. [[CrossRef](#)]
41. Yamamoto, S.; Bluhm, H.; Andersson, K.; Ketteler, G.; Ogasawara, H.; Salmeron, M.; Nilsson, A. In situ x-ray photoelectron spectroscopy studies of water on metals and oxides at ambient conditions. *J. Phys. Condens. Matter* **2008**, *20*, 184025. [[CrossRef](#)]
42. Li, W.; Kan, K.; He, L.; Ma, L.; Zhang, X.; Si, J.; Ikram, M.; Ullah, M.; Khan, M.; Shi, K. Biomorphic synthesis of 3D mesoporous SnO₂ with substantially increased gas-sensing performance at room temperature using a simple one-pot hydrothermal method. *Appl. Surf. Sci.* **2020**, *512*, 145657. [[CrossRef](#)]
43. Zhang, Y.; Li, D.; Qin, L.; Zhao, P.; Liu, F.; Chuai, X.; Sun, P.; Liang, X.; Gao, Y.; Sun, Y.; et al. Preparation and gas sensing properties of hierarchical leaf-like SnO₂ materials. *Sens. Actuators B Chem.* **2018**, *255*, 2944–2951. [[CrossRef](#)]
44. Modak, M.; Jagtap, S. Low temperature operated highly sensitive, selective and stable NO₂ gas sensors using N-doped SnO₂-rGO nanohybrids. *Ceram. Int.* **2022**, *48*, 19978–19989. [[CrossRef](#)]
45. Leghrib, R.; Felten, A.; Pireaux, J.J.; Llobet, E. Gas sensors based on doped-CNT/SnO₂ composites for NO₂ detection at room temperature. *Thin Solid Films* **2011**, *520*, 966–970. [[CrossRef](#)]
46. Bai, X.; Lv, H.; Liu, Z.; Chen, J.; Wang, J.; Sun, B.; Zhang, Y.; Wang, R.; Shi, K. Thin-layered MoS₂ nanoflakes vertically grown on SnO₂ nanotubes as highly effective room-temperature NO₂ gas sensor. *J. Hazard. Mater.* **2021**, *416*, 125830. [[CrossRef](#)]
47. Kim, H.J.; Lee, J.H. Highly sensitive and selective gas sensors using p-type oxide semiconductors: Overview. *Sens. Actuators B Chem.* **2014**, *192*, 607–627. [[CrossRef](#)]

48. Choi, M.S.; Na, H.G.; Bang, J.H.; Mirzaei, A.; Han, S.; Lee, H.Y. SnO₂ nanowires decorated by insulating amorphous carbon layers for improved room-temperature NO₂ sensing. *Sens. Actuators B Chem.* **2021**, *326*, 128801. [[CrossRef](#)]
49. Shin, H.; Jung, W.G.; Kim, D.H.; Jang, J.S.; Kim, Y.H.; Koo, W.T.; Bae, J.; Park, C.; Cho, S.H.; Kim, B.J.; et al. Single-Atom Pt Stabilized on One-Dimensional Nanostructure Support via Carbon Nitride/SnO₂ Heterojunction Trapping. *ACS Nano* **2020**, *14*, 11394–11405. [[CrossRef](#)] [[PubMed](#)]
50. Schultz, T.; Frey, N.C.; Hantanasirisakul, K.; Park, S.; May, S.J.; Shenoy, V.B.; Gogotsi, Y.; Koch, N. Surface termination dependent work function and electronic properties of Ti₃C₂T_x MXene. *Chem. Mater.* **2019**, *31*, 6590–6597. [[CrossRef](#)]